Journal of Power Sources 193 (2009) 55–64

Contents lists available at ScienceDirect

Journal of Power Sources

journal homepage: www.elsevier.com/locate/jpowsour

RedOx study of anode-supported solid oxide fuel cell

Antonin Faes[a,b,*], Arata Nakajo[a], Aïcha Hessler-Wyser[b], David Dubois[b], Annabelle Brisse[c], Stefano Modena[d], Jan Van herle[a]

[a] Laboratory of Industrial Energy Systems (LENI), Ecole Polytechnique Fédérale de Lausanne (EPFL), Lausanne, Switzerland
[b] Interdisciplinary Centre for Electron Microscopy (CIME), Ecole Polytechnique Fédérale de Lausanne (EPFL), Lausanne, Switzerland
[c] European Institute for Energy Research (EIfER), EdF, Emmy-Noether-Strasse 11, Karlsruhe, Germany
[d] SOFCPOWER S.r.l., Pergine Vals., Italy

ARTICLE INFO

Article history:
Received 20 October 2008
Received in revised form
22 December 2008
Accepted 23 December 2008
Available online 8 January 2009

Keywords:
RedOx
Anode-supported SOFC
Image analysis
Creep

ABSTRACT

The common technology for solid oxide fuel cells (SOFC) is based on a cermet (ceramic–metal composite) anode of nickel with yttria stabilized zirconia (YSZ), often used as the supporting structure. One of the main limitations of this technology is the tolerance of the anode towards reduction and oxidation ("RedOx") cycles.

In this study, two techniques are used to quantify the anode expansion after a RedOx cycle of the nickel at different temperatures. The first method considers the anode expansion above the electrolyte fracture limit by measuring the crack width in the electrolyte layer. In the second method, the anode porosity is measured using scanning electron microscopy (SEM) image quantification. The same measurement techniques are used to quantify anode expansion after consecutive RedOx cycles at constant temperature.

The quantification technique is then applied to cells tested in real stack conditions. The cell corners can undergo several RedOx cycles depending on stack design and fuel utilization. The study of such zones allows estimating the number of cycles that the anode experienced locally.

1. Introduction

As fossil fuel prices keep rising, the relevance of fuel cells steadily increases. Solid oxide fuel cells (SOFC) convert fuels effectively to high grade heat and a large electricity fraction at small power scales, keeping emissions low compared to conventional combustion systems.

A main limitation of anode-supported cell (ASC) technology, as a popular SOFC design, is its sensitivity during a reduction and oxidation cycle of the nickel-based supporting structure. Uncontrolled re-oxidation of the anode occurs at high temperature due to fuel depletion, gas leakage and at high fuel utilization. The first report on the issue was done by Cassidy et al. in the mid-1990s [1]. The problem stems from the important molar volume variation between metallic nickel and nickel oxide. During reduction, a large volume decrease occurs:

$$\Delta V_{red} = \frac{V_{Ni} - V_{NiO}}{V_{NiO}} = -41.6\% \quad (1)$$

See Table 1 [2]. This effect is exploited to increase porosity in the anode upon its first reduction. Upon re-oxidation, the volume increase:

$$\Delta V_{ox} = \frac{V_{NiO} - V_{Ni}}{V_{Ni}} \quad (2)$$

is then as high as 71.2%. During the process, nickel oxide does not reoccupy its original volume throughout the zirconia backbone. This is due to nickel sintering during utilization [3] or because nickel oxide created during re-oxidation has changed its morphology, for example, it can include higher porosity [4]. A RedOx cycle shows an irreversible expansion of the support [5]. The electrolyte will crack if the support strain exceeds 0.1–0.2% during re-oxidation [6].

The influence of the RedOx cycling temperature was observed by different groups [5,7–9]. Pihlatie et al. [5] presented an increased expansion measured by dilatometry for samples exposed to higher RedOx temperatures.

The aim of this study is to investigate the oxidation of Ni in Ni/YSZ cermet support samples in a controlled fashion in order to understand the underlying mechanisms to correlate the behavior of such controlled RedOx samples with that of cells tested in stacks, using post-mortem analysis.

* Corresponding author at: Laboratory of Industrial Energy Systems (LENI), Ecole Polytechnique Fédérale de Lausanne (EPFL), Station 9, CH-1015 Lausanne, Switzerland. Tel.: +41 21 693 6813; fax: +41 21 693 3502.
E-mail address: antonin.faes@epfl.ch (A. Faes).

0378-7753/$ – see front matter © 2008 Elsevier B.V. All rights reserved.
doi:10.1016/j.jpowsour.2008.12.118

Table 1
Nickel and nickel oxide molar mass, specific mass and molar volume [2].

	NiO	Ni
M (g/mol)	74.71	58.71
ρ (g/cm^3)	6.6	8.9
V (cm^3/mol)	11.32	6.60

2. Experimental

The anode supports (ca. 0.25 mm thick) were produced by tape-casting (HTceramix SA, Switzerland) using 55 wt% NiO and 45 wt% YSZ, and then co-sintered with a ca. 4 μm 8YSZ electrolyte to produce half-cells [10–12].

Thermogravimetric analysis (TGA Mettler-Toledo) was used to analyze weight variation upon reduction and oxidation at constant temperature. Fragments of half-cells of about 10 mm^2 were transferred to alumina crucibles. Reduction was carried out under a flow of 200 ml/min of dry 9% H_2 in N_2. 200 ml/min of dry air flow was applied for the oxidation step. The duration of the reduction and oxidation steps was chosen as the time required to reach mass stabilization. This was 8 h for 600 °C, 2 h for 700 °C and 1 h for 800, 900 and 1000 °C.

Complete cells comprised a composite cathode of lanthanum strontium manganite (LSM) and YSZ, screenprinted and sintered onto the thin electrolyte layer. A current collecting layer of lanthanum strontium cobaltite (LSC) was screenprinted onto the cathode and sintered in situ. The cells were tested in stack conditions (so-called R-design from HTceramix SA [13]) using Cro-Fer22APU interconnects. Compressive sealing was used to separate the air fuel manifolds.

A scanning electron microscope (SEM) FEI XL30 SFEG was used for microstructural observations between 1 and 30 kV with a field emission gun (FEG). The microscope was equipped with a secondary electron (SE) detector, a back scattered electron (BSE) detector, a through lens detector (TLD) and an energy dispersive X-ray spectrometer (EDS).

In order to look inside the microstructure of samples after a RedOx cycle, a dual beam SEM/FIB (focused ion beam) model FEI Nova 600 Nanolab was used. The cermet cross-sections were prepared by milling the sample with Ga^+ ions at an acceleration voltage of 30 kV and a decreasing current from 20 nA to 100 pA. Imaging was carried out with FIB at 30 kV and 50 pA using the Everhard–Thornley SE detector.

As the samples could not withstand a full RedOx cycle at 800 °C without dramatic failure, a direct strain measurement such as dilatometry could not be used. To determine anode expansion, two indirect techniques have been applied, one focusing on electrolyte cracks and the second on the anode porosity. For image analysis of cracks in the electrolyte, the working distance (5 mm), magnification (1200×) and acceleration voltage (15 kV) were kept constant for the full batch of observations. The widths of all cracks were summed up and related to the total length measured [14]. For each picture, a total length of 400 μm in both directions was analyzed. Two pictures for each temperature of oxidation were considered.

For porosity measurement, sample preparation is done by mechanical polishing after impregnation with epoxy (Fluka®). Image treatment is done by a grey level threshold to extract the porous phase, then the surface of this phase is compare to the total surface of the image. This image analysis is done using a Mathematica® code developed in-house [15]. The majority of samples observed here are in oxidized state. For the others, the state will be specified.

Finite-element analysis (FEA) is used to calculate the stresses in the electrolyte and anode-support layer during a RedOx cycle. A two-dimensional, plane strain model was implemented in ABAQUS® [16]. The mesh was made of second-order, reduced-integration elements (CPE8R).

Table 2
Thermomechanical constant used for the FEM calculations.

	Young modulus, E (GPa)	Coefficient of thermal expansion, TEC (K^{-1}) [19]
Electrolyte (8YSZ)	157 (800 °C) [18]	10.5×10^{-6}
NiO–8YSZ	161 (RT) [18]	12.0×10^{-6}
Ni–8YSZ	96 (RT) [20]	11.0×10^{-6}

3. Results

3.1. Re-oxidation strain limit of anode-supported electrolyte (ASE)

The strain limit of an anode-supported cell before cracking the electrolyte (ε_{lim}) is calculated using finite element modeling (FEM) and failure statistics. ABAQUS® calculated the stresses in the electrolyte due to, first, the mismatch in the coefficients of thermal expansion (CTE) between the YSZ electrolyte and NiO–YSZ anode and, second, due to the anode expansion during a RedOx cycle. The thermal stresses are built up between the zero-stress temperature (1200 °C [17]) and the RedOx temperature. Thermomechanical values used for the calculation are given in Table 2 [18–20].

Failure probability for ceramics is based on Weibull statistics [21] and can be expressed as a function of the stress (σ) and the volume tested (V_{test}) (Eq. (3)):

$$P_f = 1 - \exp\left(-\left(\frac{\sigma}{\sigma_0}\right)^m \frac{V_{test}}{V_0}\right) \quad (3)$$

where σ_0 is the Weibull strength at a probability of failure (P_f) of 0.632, m is the Weibull modulus and V_0 is the effective tensile volume during the strength tests. Atkinson and Selçuk measured by the ring-on-ring tesing method for YSZ at 800 °C, σ_0 = 156 MPa with m = 8.6 [18]. From the specimen and setup size, an effective tensile volume (V_0) of 1.2538 mm^3 was calculated using ASTM C1499-04 [22]. Fig. 1 presents the probability of failure of a 4 μm thick electrolyte depending on the strain of the anode support during re-oxidation at 800 °C. The re-oxidation strain at 100% probability of electrolyte failure for a 10 mm^2 sample (i.e., in our case the TGA samples) is $\varepsilon_{lim(100\%)}$ = 0.18%. This is close to the maximal anode expansion calculated from Klemensø (0.17%) based on analytical stress calculations in a multilayer [23]. Sarantaridis and Atkinson

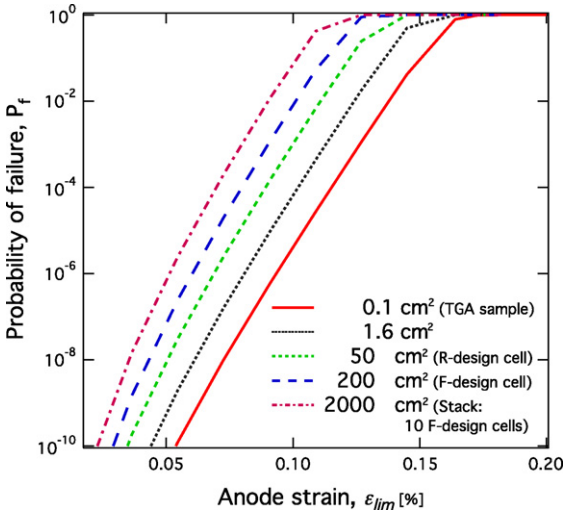

Fig. 1. Probability of failure of the electrolyte (thickness 4 μm) versus the re-oxidation anode strain for different sample sizes.

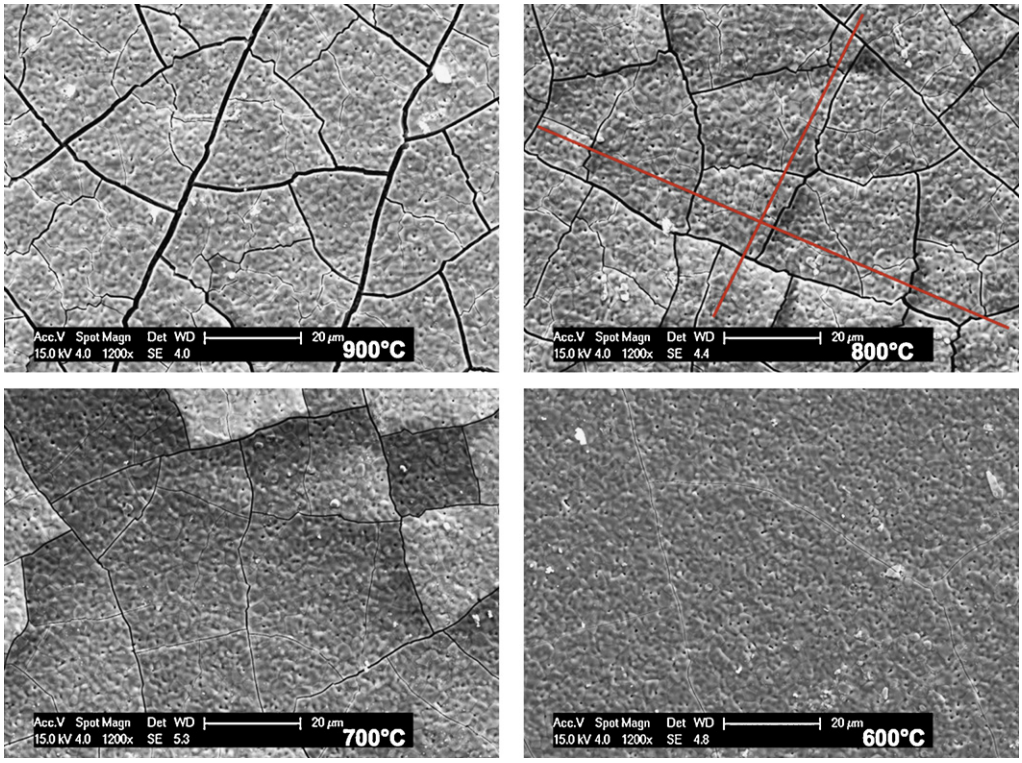

Fig. 2. Typical SEM images using secondary electron detector used for expansion measurements (half-cells after RedOx cycle at different temperature).

obtained a maximal strain between 0.1 and 0.2% based on energy fracture mechanics [6].

From another perspective, if it is assumed that only one sample out of 10,000 is allowed to break ($P_f = 10^{-4}$), then the strain limit has to be reduced to $\varepsilon_{lim(0.01\%)} = 0.12\%$.

The Weibull approach gives the probability to find a critical flaw in a certain volume. The larger the sample, the lower the maximum anode strain. The maximum admissible re-oxidation strain decreases to 0.12% for a total cell surface in a stack of 2000 cm^2. This explains in part the higher RedOx sensitivity of a stack compared to smaller test samples [7].

Due to residual stresses, ε_{lim} varies with temperature of oxidation. $\varepsilon_{lim(100\%)}$ is 0.165% at 900 °C and increases to 0.21% at 600 °C, as compressive stresses build up in the electrolyte by lowering the temperature.

It is important to note that ε_{lim} will be strongly affected by the accuracy of Weibull parameters as well as the exact test volume.

3.2. First method for ASE strain measurement: electrolyte crack width (single RedOx cycle at different temperatures)

From the electrolyte crack widths, it is possible to calculate the expansion of the anode. This approach was briefly presented by Robert et al. [14]. Four pictures at the same magnification are presented in Fig. 2 to qualitatively show the difference in electrolyte cracking depending on the re-oxidation temperature. The number of cracks as well as the fracture widths increase with increasing temperature. The electrolyte fracturing seems to be oriented in two approximatively perpendicular directions (see the superimposed lines in Fig. 2).

The anode expansion due to re-oxidation ($\varepsilon_{Anode,crack}$) is calculated using Eq. (4). As the electrolyte is still under stress (no delamination observed on cross section view), the ε_{lim}-value is added to the measurement. During the cooling after the RedOx cycle, the crack width will decrease due to the thermal expansion difference between anode support and electrolyte:

$$\varepsilon_{Anode,crack} = \varepsilon_{\lim} + \frac{\sum_i w_{c,i}}{L_{tot}} + \Delta TEC(T_{RedOx} - T_{RT}) \quad (4)$$

where $w_{c,i}$ is the width of crack i, L_{tot} is the total line length measured on the picture, ΔTEC is the thermal expansion coefficient difference between anode and electrolyte layer (Table 2), T_{RedOx} is the temperature of the RedOx cycle and T_{RT} is room temperature.

The results are summarized in Fig. 3. The expansion of the studied support is only 0.42% when the oxidation occurs at 600 °C, but 1.52% at 700 °C, 2.86% at 800 °C, and more than 4.4% at 900 °C.

A linear extrapolation in Fig. 4 is used to calculate at which temperature the expansion of the anode is low enough that no cracking

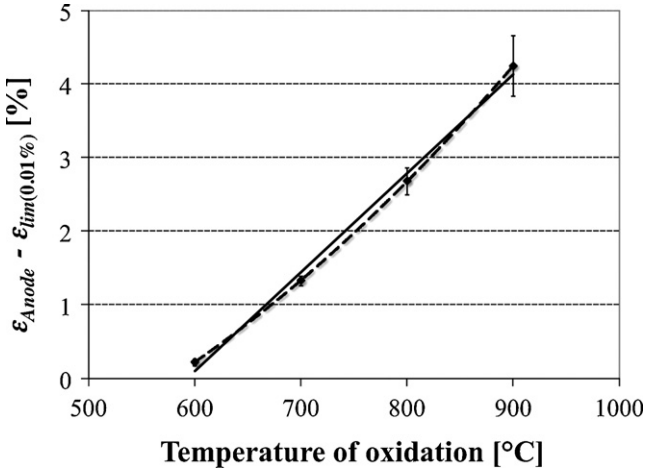

Fig. 3. Anode strain beyond the electrolyte cracking limit ($\varepsilon_{Anode} - \varepsilon_{lim}$ in %) after one RedOx cycle at different temperatures, measured from electrolyte crack widths. The solid line is a linear extrapolation ($R^2 = 0.994$) and the dashed line is the quadratic extrapolation ($R^2 = 1$).

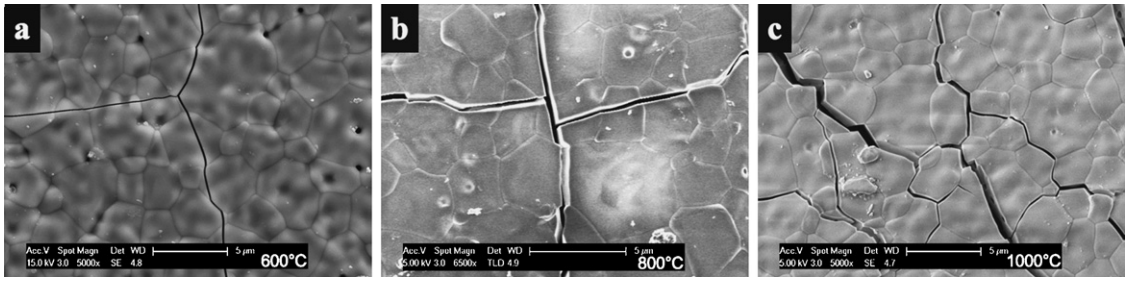

Fig. 4. Secondary electron SEM images presenting the morphology of the half-cell electrolyte cracks appearing at different re-oxidation temperatures (a) 600 °C, (b) 800 °C and (c) 1000 °C.

of the electrolyte occurs ($\varepsilon_{Anode} < \varepsilon_{lim(0.01\%)}$). Here, the maximum strain limit is fixed such that one sample out of 10,000 will fail ($P_f = 0.01\%$, in equation 1) and its value is $\varepsilon_{lim(0.01\%)} = 0.12\%$ for a RedOx temperature of 800 °C (see Fig. 1). This temperature is designated as "$T_{safe,lin}$" and is equal to 592 °C. If the extrapolation is taken as quadratic instead of linear, then $T_{safe,quad} = 578$ °C. When the error in the measurements is taken into account, the safe temperature should be as low as 581 and 557 °C for linear and quadratic extrapolation, respectively. To confirm this prediction, a RedOx cycle was performed on a fresh sample at 550 °C for 9 h (until TGA mass stabilization). It did indeed not show any crack in the electrolyte.

Different crack types were observed in the electrolyte depending on the RedOx cycling temperature (Fig. 4). At 600 °C, the fractures are quasi straight and go through the grains (trans-granular or intra-granular cracks). At 1000 °C, although straight cracks are still present, larger inter-granular ones are visible. In particular, a single grain can be detached from the surrounding grains (at the center Fig. 4c). YSZ electrolyte cracks upon re-oxidation change from intra-granular at low temperature to inter-granular at higher temperature [24]. At 800 °C, a mixed behavior is observed in Fig. 4, as both inter- and trans-granular cracks are present.

Fig. 5 presents the evolution of a crack after the first re-oxidation, second reduction and a second re-oxidation, all at 600 °C. It is interesting to observe that the crack closes back after re-reduction (Fig. 5c), when tensile stresses in the electrolyte are released and turn to compressive. It can be expected from these observations that if cracks in the electrolyte are small enough, they will close again and no leakage will occur between anode and cathode atmospheres. However, the crack width doubles between the first and the second re-oxidation from 40 to 80 nm (Fig. 5b and d), showing the irreversibility of RedOx cycling even at low temperature.

3.3. Second method for ASE strain measurement: porosity from image analysis (single RedOx cycle at different temperatures)

Fig. 6 presents qualitative and quantitative microstructural evolution after one RedOx cycle at different temperatures. A cycle at 700 °C does not seem to influence the microstructure much beyond that of 600 °C, but after a RedOx cycle at 800 °C and 900 °C the porosity increases from 0.8 to 4.6% and 10.5%, respectively. The increase in porosity is reflected by a volume increase of the anode support. We can calculate the isotropic anode strain ($\varepsilon_{Anode,poro}$)

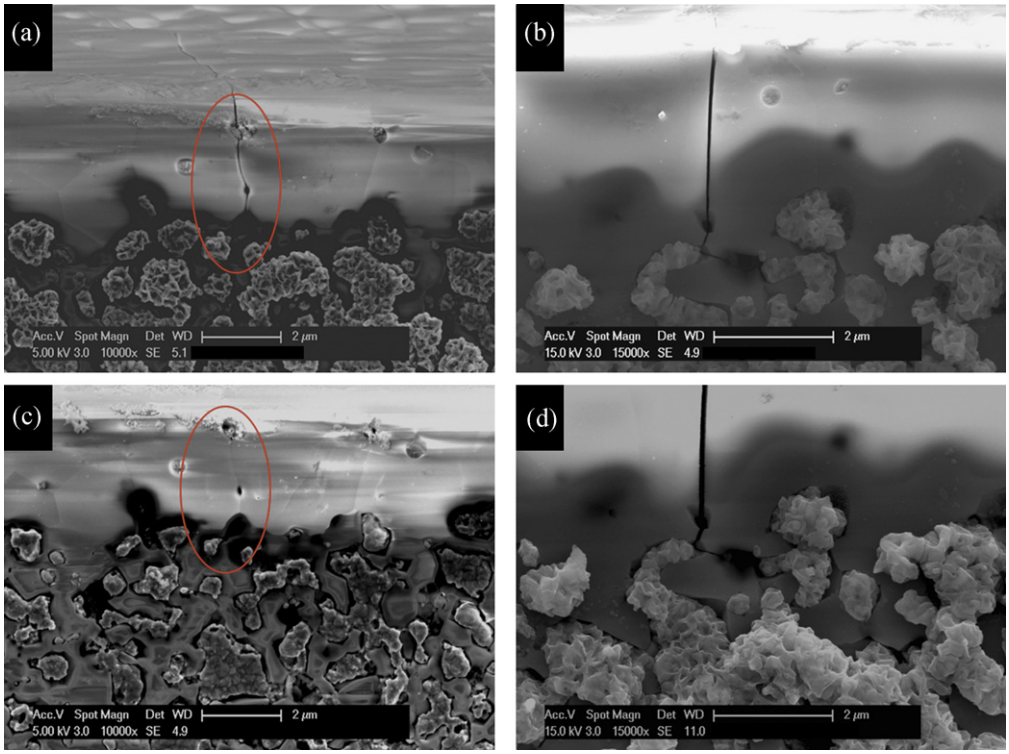

Fig. 5. Half-cell electrolyte crack evolution after first re-oxidation (a and b), second reduction (c) and second re-oxidation at 600 °C (d). The same fissure from the first oxidation (a) closed back after the next reduction (c). All pictures are secondary electron SEM images.

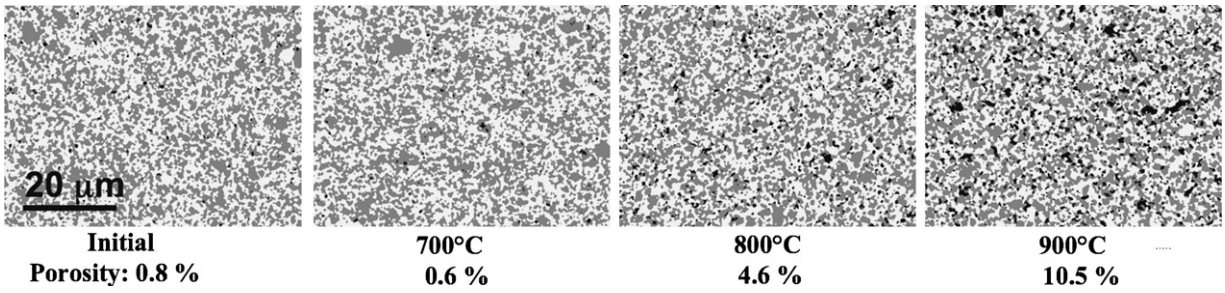

Fig. 6. Half-cell anode microstructure after one RedOx cycle at different temperatures and the corresponding porosity (phase color: black = pores, white = nickel oxide, grey = YSZ).

from the increase in volume simply by

$$\varepsilon_{Anode,poro} = \sqrt[3]{V_s + \Delta V_p} - 1 = \sqrt[3]{V_s + V_{pf} - V_{pi}} - 1 \quad (5)$$

where $V_s = 100\%$ is the solid volume, V_{pi} is the volume of initial porosity (0.8%) and V_{pf} is the volume of porosity after the RedOx cycle. Anode strains from such porosity measurement after one RedOx cycle are 0, $1.25 \pm 0.13\%$ and $3.13 \pm 0.32\%$ for 700, 800 and 900 °C, respectively. The comparison of these values to the expansion measured from electrolyte cracking shows a roughly constant absolute difference of about 1.3% (see Fig. 3). This difference will be discussed later.

3.4. Multiple RedOx cycling at 800 °C (methods 1 and 2)

Subsequent RedOx cycles were done on different samples from the same tape batch at a constant temperature in the TGA furnace. For each number of cycles, one sample was produced. The "one cycle" and "seven cycles" samples were replicated to check reproducibility of the experiment. The measurement methods are the same as the ones presented in Sections 3.2 and 3.3.

The experimental strain measurements in Fig. 7 are fitted with an exponential model similar to a charging capacitor [15]:

$$\varepsilon_{Anode}(N) = \varepsilon_{\max}\left(1 - \mathrm{Exp}\left(-\frac{N}{\tau}\right)\right) \quad (6)$$

where ε_{max} is the maximum limit of strain for an infinite cycle number, N is the number of RedOx cycles and τ is a characteristic exponential constant corresponding to the number of cycles needed to reach 63.2% of the maximum strain (i.e. $1 - \mathrm{Exp}(-1) = 0.632$).

For both anode strain measurements, the τ value is roughly 3 within the error range (see Table 3). The maximum strain, however, for the crack measurement technique is almost twice that of the porosity measurement technique. This problem was also observed during variation of the re-oxidation temperature (Sections 3.2 and 3.3) and will be discussed in Section 4.1.

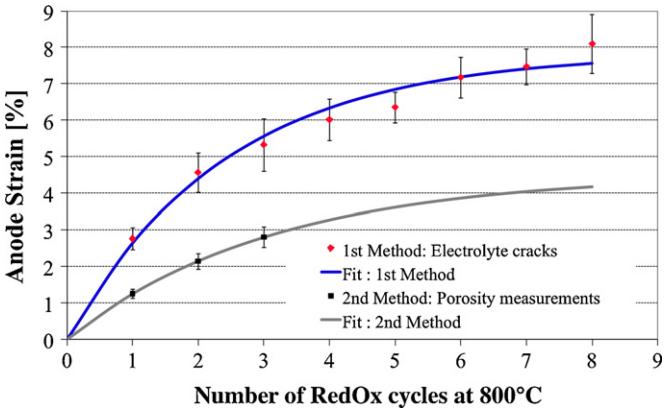

Fig. 7. Comparison of anode strain measured from electrolyte crack widths and by porosity measurements from image analysis. The consecutive RedOx cycles were done isothermally at 800 °C.

Table 3
Exponential model constants for anode support strain increase with consecutive RedOx cycles at 800 °C (τ is the number of cycles needed to reach 63% of the maximal strain, ε_{max}).

	Porosity measurement	Cracks in electrolyte
τ [Nbr of Redox cycle]	3.0 ± 0.1	2.5 ± 0.4
ε_{max} (%)	4.5 ± 0.1	7.9 ± 0.5

3.5. Application of method 2 to a cell tested in a stack

Comparison of the behavior of isolated cermet samples under controlled RedOx cycling of half cells, discussed above, with that of a real cell in a stack is used to extract an equivalent number of RedOx cycles endured by the cell during utilization, depending on location. Fig. 8 shows images of such a cell.

The colors of the cell on the optical image indicate the oxidation state of nickel. Metallic nickel is grey and stoichiometric NiO is

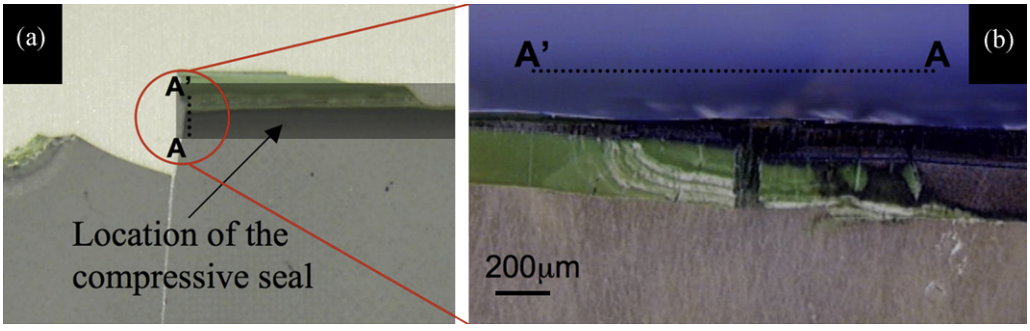

Fig. 8. Optical images of the cell tested in a stack (530 h, 800 °C). (a) Planar view of the anode side and (b) cross-section (with indication of the location of the compressive seal during operation). Nickel oxide is green and metallic nickel grey. White lines are highly porous regions.

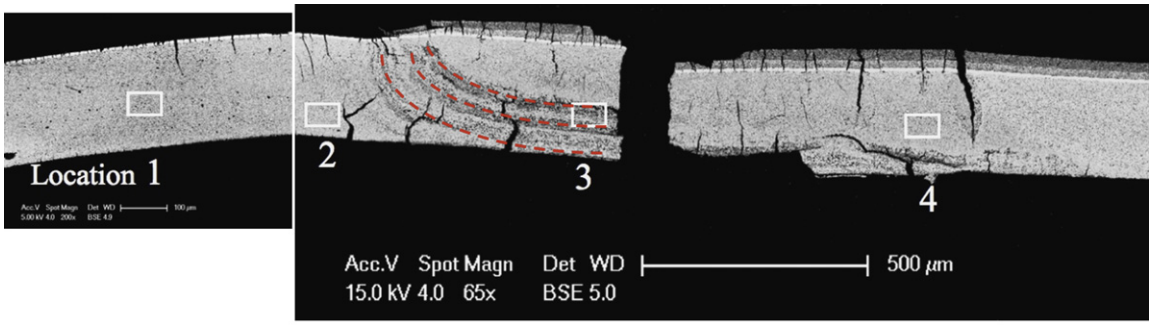

Location	Porosity [%]
1	9.1
2	13.8
3	51.9
4	10.3

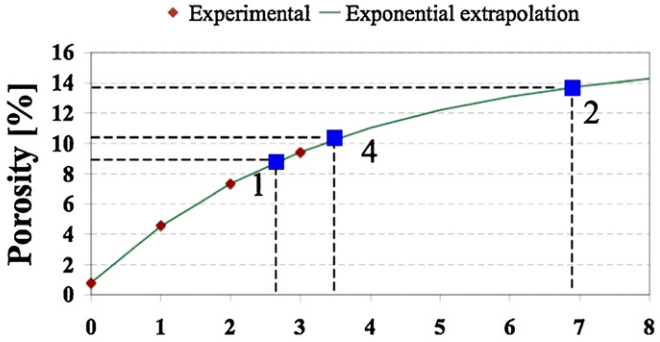

Fig. 9. Backscattered electron image from cross section of the full cell showed in Fig. 8 with location of the porosity measurement. The graph compares porosity measurements with values obtained from consecutive RedOx cycling at 800 °C. Porosity extrapolation is based on Eq. (6). Location 1 and 4 "saw" about 3 and 4 RedOx cycles at 800 °C, respectively. Location 2 supported 7 RedOx cycles at 800 °C (supposing isothermal conditions).

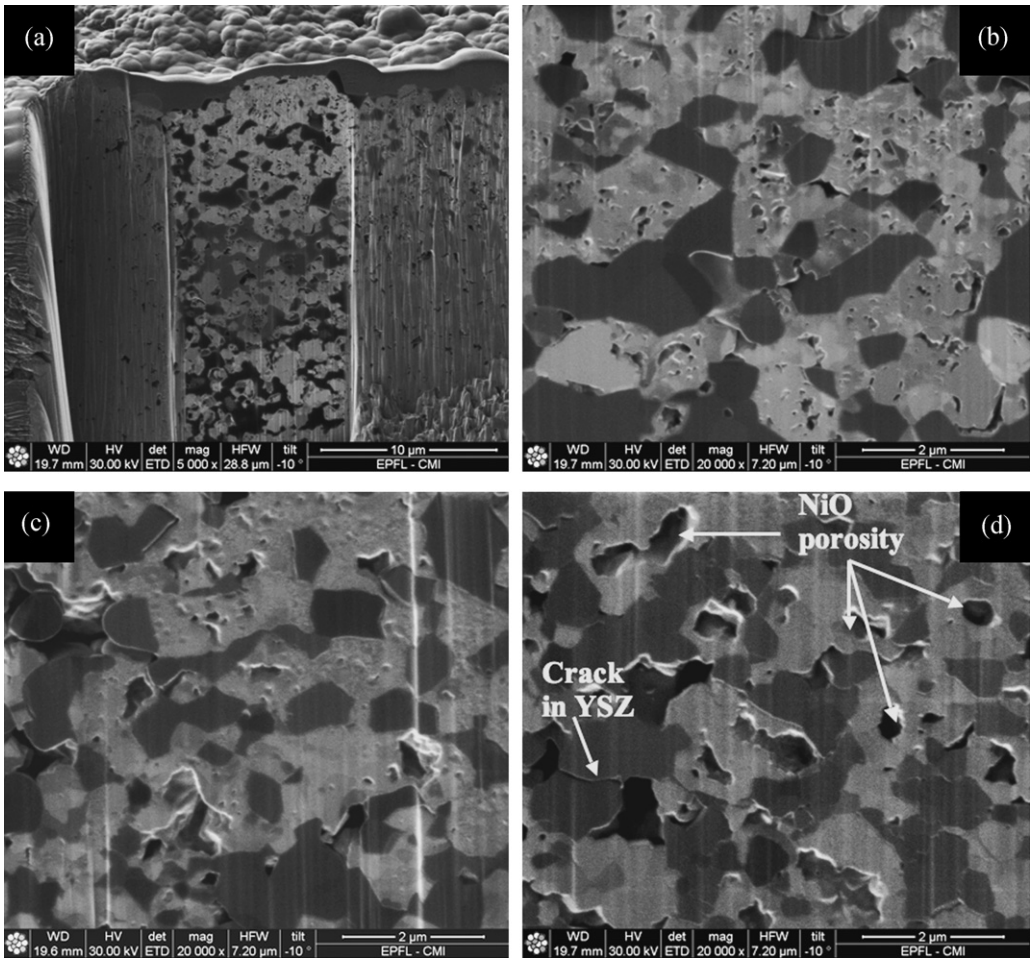

Fig. 10. Secondary electron image from focused ion beam (FIB) cross-section from half-cells after one RedOx cycle (a) at 550 °C (lower magnification), (b) at 550 °C (higher magnification), (c) at 800 °C and (d) at 1000 °C. NiO contains small pores after a RedOx cycle at 550 and 800 °C but a single big pore after a RedOx cycle at 1000 °C. Dark grey is YSZ and light grey is NiO. The vertical lines come from the FIB milling process ("curtain effect").

green. Ni_2O_3 is known to be black but, in fact, under-stoichiometric $Ni_{1-\delta}O$ changes from green to black, through dark green with increasing δ [8]. The inner part of the anode is under fuel atmosphere with low partial pressure of oxygen whereas the outer part of the cell is exposed to surrounding air in the furnace. As the anode and the compressive seals used in stacking are porous, fuel and oxygen can diffuse and create a combustion zone [25]. This combustion increases locally the temperature and creates a RedOx front (localized by the red dashed lines in Fig. 9). Outside of the anode compartment, nickel is oxidized due to air atmosphere in the furnace (left side of Fig. 9). Metallic nickel is present in the fuel compartment within the RedOx front (right side of Fig. 9). As fuel utilization (FU) changes, the position of this RedOx front moves. At high FU, the RedOx front is shifted inside the cell compared to the case at low FU (for example at open circuit voltage: OCV) where the RedOx front is closer towards the cell edge. Therefore, operating a current–voltage (*IV*) scan on the stack can correspond to re-oxidizing the outer cell parts. This process was described by Wuillemin et al. [25].

The cell analyzed in Fig. 9 comes from a stack tested for 530 h at 800 °C, at three different FU (40, 50 and 60%). The test underwent 4 *IV*-scans. It is suggested that these different FU give rise to the three curved lines visible on the cross-section (white lines in Fig. 8b and red dashed lines in Fig. 9), corresponding to the location of combustion. The most external line (on the left) corresponds to the lowest FU. These lines are structured with high porosity (up to 50%, location 3 in Fig. 9).

4. Discussion

4.1. Comparison of the 2 methods for ASE strain measurement

A deviation between the two measuring methods is observed. The 1st method, using crack width, gives a systematically higher value, outside of the error bars of both methods. At low temperature (600–700 °C), the 2nd method, anode porosity increase, does not show any strain of the support even if the electrolyte cracks.

Two main reasons for this deviation are proposed:

1. Sample preparation (for method 2).
2. Creep during oxidation.

4.1.1. Sample preparation

The second method needs mechanical polishing of the composite. During this process, closed porosity can be filled up with polished materials (NiO and YSZ), as this porosity does not get impregnated with resin during normal sample preparation for microscopy observation. To observe closed porosity, focused ion beam (FIB) milling can be used instead. This micromachining was originally used for semiconductor applications like integrated circuits and micro-electro-mechanical systems (MEMS) [26]. Fig. 10 shows the composite microstructure after one RedOx cycle at constant temperature prepared using FIB milling. After the RedOx cycle, nickel oxide particles contain pores. The lower the RedOx temperature, the smaller the pore size. At 550 °C the pores are well dispersed in the nickel oxide particles whereas at 1000 °C the NiO is dense and only one big central pore is present in the grain. At high temperature the NiO grain structure is similar to hollow spheres. At intermediate temperature (800 °C) the porosity arrangement is between those obtained at the lower and higher temperatures.

Small pores in nickel oxide created at low temperature will be filled up easier than lager ones. Then $\varepsilon_{Anode,poro}$ from the second method will be underestimated for low temperature RedOx cycles. This is a reason why no expansion from the porosity method is measured at low temperature (600 °C–700 °C). Quantitative image analysis from FIB cross sections alone is difficult and not representative, as the surface is reduced to only a few μm^2.

A deeper analysis of the observations using FIB will be reported elsewhere.

4.1.2. Creep during oxidation

Malzbender et al. [27] observed convex curvature to the electrolyte side during in situ oxidation of Ni–YSZ half-cells. This can be due to the fact that oxidation may induce creep in the zirconia structure [24,28] at the anode support side due to high exothermicity of nickel oxidation ($\Delta H_{298\,K} = -239.8$ kJ/mol of NiO) [29]. As the oxidation front follows the thickness of the support, the reaction slows down and the thickness of the re-oxidized layer increases; therefore no additional creep occurs. Finally, the electrolyte side opposite of the support is under tension due to initial creep; this induces more expansion of the electrolyte surface.

Creep is the plastic deformation of materials under long-term stress. In the initial stage, or primary creep, the strain is relatively high, but slows down with increasing strain. Then the strain rate becomes quite constant (secondary or steady-state creep). Finally, in tertiary creep, the strain rate increases exponentially with strain.

For the secondary stage, the creep rate, $\dot{\varepsilon} = d\varepsilon/dt$, depends on temperature, T, and the applied stress, σ. It is generally described by the phenomenological relation [24]:

$$\dot{\varepsilon} = A\sigma^n \exp\left(-\frac{Q}{RT}\right) \tag{7}$$

where A is a constant, n is the stress exponent for creep, Q is the activation energy and R is the gas constant. Dense single crystal yttria stabilized zirconia with a composition between 9.5 and 21 mol% of Y_2O_3 (9.5–21 YSZ) was tested between temperatures of 700 and 1600 °C [30–32]. Polycrystalline 8YSZ was tested between 925 and 1000 °C and gave an exponent value of 0.7 and an activation energy of 320 kJ/mol [24]. Gutierrez-Mora et al. [28] presented compressive creep deformation of a 40 vol.% nickel with 60 vol.% 8YSZ porous composite between temperatures of 1000 and 1200 °C. They found a stress exponent, n, between 1.2 and 1.9, suggesting that the deformation is controlled by a diffusion mechanism. At a stress under 20 MPa and a temperature above 1100 °C, the deformation rate is as high as $5 \times 10^{-5}\ s^{-1}$, corresponding to a deformation of 0.3% in only 1 min.

Ettler et al. [7] observed a sharp border between the oxidized and reduced parts of anode samples, for oxidation temperatures higher than 700 °C. In this way, stresses can be qualitatively described by the classical case of two beams subjected to different thermal strains. Bending of the bilayer is prevented and no interfacial stresses are considered. The oxidation front starts from only one side of the support as the opposite side is covered by the dense electrolyte. The force equilibrium is given by

$$\sigma_{ox} t = -\sigma_{red}(1 - t) \tag{8}$$

see Fig. 11a. Hence, σ_{ox} can be computed using force equilibrium and identical length for both beams (no curvature):

$$\sigma_{ox} = -\frac{E_{ox}E_{red}(1-t)}{E_{ox}t - E_{red}(1-t)}\varepsilon_{ox} \tag{9}$$

where E_{ox} and E_{red}, are the Young's moduli of the oxidized and the reduced layer, respectively, ε_{ox} is the strain due to oxidation and t is the thickness of the oxidized layer. Fig. 11b presents the stress in the layers as function of the thickness of the oxide layer. This model shows that compressive stress in the oxide layer decreases as the reaction moves forward, when its thickness increases.

During the reaction, the temperature of the sample is not equal to the temperature of the furnace as nickel oxidation is exothermic. Nickel oxidation follows parabolic kinetics (Wagner mechanism) as does the cermet oxidation [8]. For a parabolic reaction, the rate is

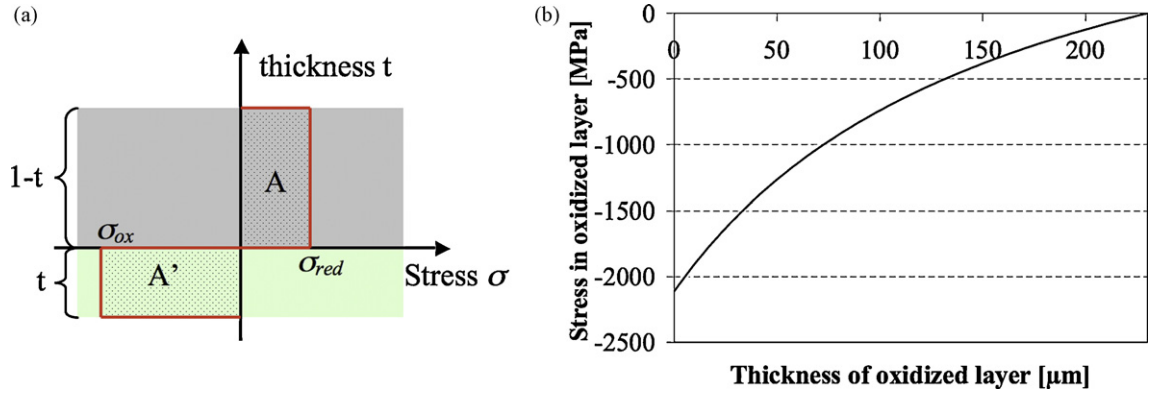

Fig. 11. (a) Schematic view of stress in the layers during oxidation of the anode support (green is oxidized and grey is reduced). (b) Stress in the oxide layer during oxidation at 800 °C (1.25% of strain) versus the thickness of the oxide layer. (For interpretation of the references to color in this figure legend, the reader is referred to the web version of the article.)

faster at the beginning and slows down due to the diffusion process. Complete anode support oxidation takes only 25 min at 800 °C. A temperature increase of 1678 °C is calculated from the adiabatic reaction of an anode support (final composition of 55 wt% NiO and 45 wt% YSZ) using Eq. (10):

$$-n_{NiO}\Delta H_{ox,Ni} = n_{NiO}\left(\int_{1073\,K}^{T_{fusion}} C_{p,m,NiO,s}\,dT + \Delta H_{fusion,NiO}^{T_{fusion}} + \int_{T_{fusion}}^{T_{adiab}} C_{p,m,NiO,l}\,dT\right) + n_{ZrO_2}\left(\int_{1073\,K}^{1420\,K} C_{p,m,ZrO_2,\alpha}\,dT + \Delta H_{\alpha\rightarrow\beta}^{1420\,K} + \int_{1420\,K}^{T_{adiab}} C_{p,m,ZrO_2,\beta}\,dT\right) \quad (10)$$

where n_{NiO} and n_{ZrO_2} are the number of moles of NiO and zirconia, respectively, $C_{p,m}$ is the molar heat capacity (at a constant pressure), $\Delta H_{ox,Ni}$ is the enthalpy of oxidation of nickel ($Ni + 1/2O_2 \Rightarrow NiO$), $\Delta H_{fusion,NiO}$ is the enthalpy of fusion of nickel oxide (the melting point of NiO is T_{fusion} = 1990 °C), $\Delta H_{\alpha\rightarrow\beta}$ is the enthalpy for zirconia phase change (from α to β phase) and T_{adiab} is the calculated final temperature for the adiabatic reaction (T_{adiab} = 2478 °C). $C_{p,m}$ is calculated from the following equation:

$$C_{p,m} = a + bT \quad (11)$$

The heat capacity for pure α and β-zirconia and solid and liquid NiO were used for the calculation [33]. Thermodynamic constants are given in Table 4.

When oxidation kinetics are fast (at high temperature and at the beginning of the reaction), the sample temperature will increase. As creep is influenced by temperature (see Eq. (7)), it will be higher during the initial stage of the reaction (kinetics follow a parabolic law [8]). Also at elevated re-oxidation temperature, the creep will be higher.

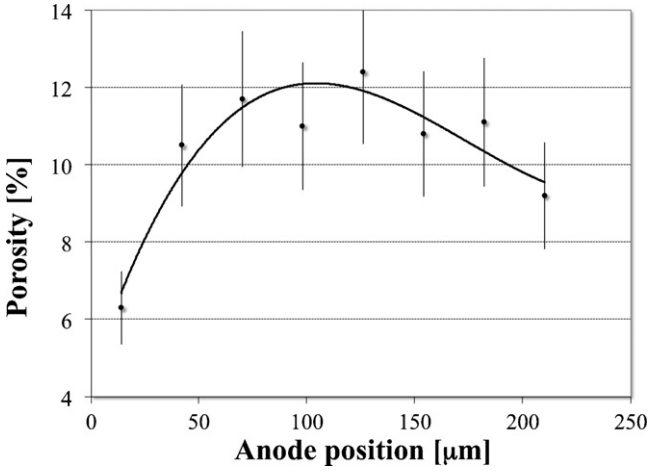

Fig. 12. Porosity versus anode thickness position for one RedOx cycle at 900 °C (0 μm corresponds to the outer surface of the anode and 230 μm to the electrolyte/anode interface). The line is a help to guide the eye.

As densification during creep deformation occurred in the composite [28], porosity measurements were done along the thickness of the sample using image analysis of pictures taken at 3500× magnification. This represents a measurement every 26 μm. The results are presented in Fig. 12 for a sample after one RedOx cycle at 900 °C. The porosity at the bottom of the anode is about half the porosity in the center of the anode. This confirms higher deformation at the outer layer of the sample during oxidation. A lower value is again obtained close to the electrolyte. This can be explained by compression in the anode after re-oxidation due to the electrolyte layer. The same measurement on an original sample as sintered did not show any variation in porosity along the thickness.

Another interesting observation is the presence of cracks at the bottom of the anode support (see Fig. 13). During the oxidation of the first layer, creep and densification made this layer shrink. At the center of the support, no creep will occur and the support will

Table 4
Thermodynamic constants for NiO and ZrO_2. $C_{p,m}$ is the molar heat capacity (at constant pressure), ΔH_{ox} is the enthalpy of oxidation of nickel ($Ni + (1/2)\,O_2 \Rightarrow NiO$ at 800 °C) and ΔH_{fusion} the enthalpy of fusion of nickel oxide (melting point of NiO is T_f = 1990 °C [2]). $C_{p,m}$ is calculated from equation $C_{p,m} = a + bT$ [33].

	a (J mol^{-1} K^{-1})	b (J mol^{-1} K^{-2})	$\Delta H_{ox,Ni}$ (kJ mol^{-1})	ΔH_{fusion} (kJ mol^{-1})	$\Delta H_{\alpha\rightarrow\beta}$ (kJ mol^{-1})
NiO solid	46.81	8.46×10^{-3}	239.8 [29]	50.66 [33]	
NiO liquid	59.87				
α-ZrO_2	57.80	16.67×10^{-3}			4.75 [33]
β-ZrO_2	78.63				

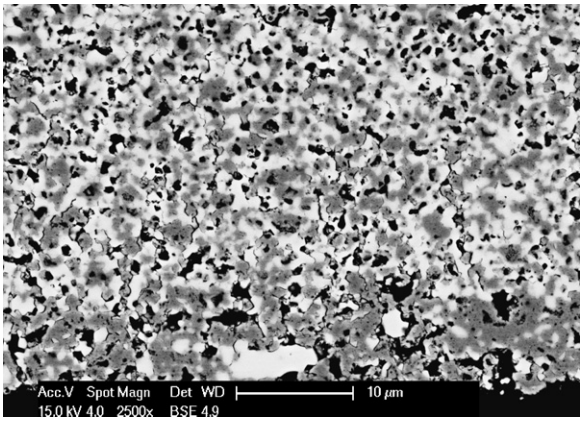

Fig. 13. Backscattered electron SEM image of the bottom layer from anode support half-cell after one RedOx cycle at 900 °C. Vertical cracks are produced due to the tensile stress at the bottom of the anode (black = porosity, grey = NiO and white = YSZ).

freely expand. This will induce tensile stresses and fissures in the initial crept layer exposed earliest to re-oxidation.

The tension in the anode bottom layer makes the electrolyte side expand further due to curvature. This can explain the different results between the two methods for anode strain measurement using electrolyte crack widths or porosity image analysis.

4.2. FEM calculation and experimental results

A SEM image of a half-cell after one RedOx cycle at 800 °C is qualitatively compared to a FEM calculation in Fig. 14. ABACUS® was used to calculate the stress around a crack formed in the electrolyte layer. Cracks were placed according to the SEM image and the strain is applied to the anode layer.

The stress distribution in the electrolyte and anode layers can be modeled using finite element analysis. The oxidation strain exceeds the thermal strain and thus induces tensile stresses in the electrolyte, which leads to cracking of the latter layer. Even though the stress state in the anode is compressive, the fissures propagate a few microns through the anode layer. The cracking of the electrolyte releases stresses, which turn from tensile to compressive, between two main cracks, when moving upwards from the anode/electrolyte interface. This can prevent the propagation of cracks initiated at the interface, as illustrated in Fig. 14b.

4.3. Application to a cell tested in a stack

Using method 2 (porosity measurement), it is possible to estimate the number of RedOx cycles undergone by the different regions of a cell in real stack testing conditions (see Fig. 9).

The number of RedOx cycles obtained in this way was between 3 and 4 for locations away from the combustion zone (1 and 4), which is consistent with the number of *IV* scans (4 in total). Location 1 was under the seal but at the air side with respect to the combustion area under normal condition (FU = 40–60%). Location 4 was at the fuel side but was oxidized due to air leakage from the cathode (fissures at the right in Fig. 9). Location 2 in this way would lead to hypothetically seven RedOx cycles at 800 °C. It is possible that a small fluctuation of fuel flow or current density put this location in the RedOx front. Another explanation for the higher anode porosity at position 2 is the exposure to elevated temperature closer to the combustion zone and consequently a worsened effect of the RedOx cycle. For example, the increase in porosity is higher after one cycle at 900 °C (10%) than after three cycles at 800 °C (9%) (cf. Figs. 3 and 7).

Location 3 is at the position of combustion. Here porosity is higher than 50%, which means that high temperature and the high steam fraction made the nickel oxide phases diffuse out and leave large porosity behind. As the YSZ backbone is already broken from earlier RedOx cycles, the structure is no longer maintained.

The real conditions of use of a cell are thus very extreme, in the particular cell and flow design of the studied stack. Solutions were implemented to modify the design and flow pattern and to change sealing [13,34,35], which have dramatically improved the durability, and cell appearance after testing.

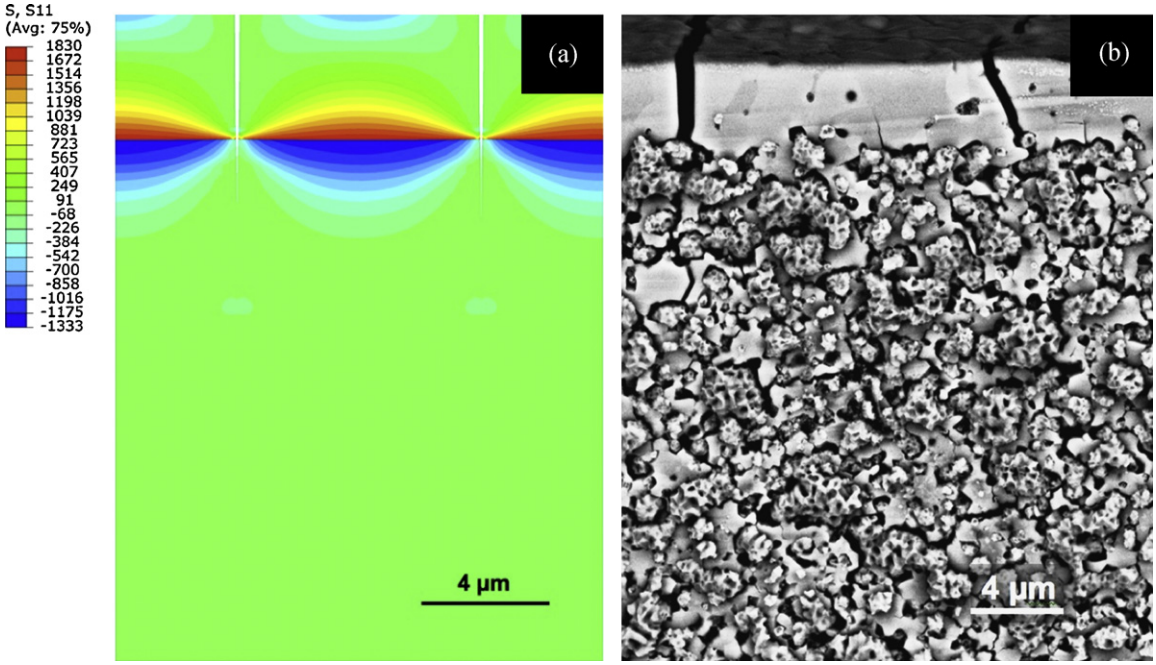

Fig. 14. (a) Finite element model (FEM) stress calculation (given in MPa) between two fissures for an anode strain of 1.25% shows tensile stress at electrolyte bottom and compressive stress at the top. (b) Secondary electron SEM cross-section image of a half-cell after one RedOx cycle at 800 °C.

5. Conclusions

This work shows two different methods based on image analysis to measure the expansion of a tape cast Ni–YSZ anode support (HTceramix® SA) during RedOx cycling. A direct method like dilatometry could not be used as the anode support electrolyte (ASE) could not withstand RedOx cycles higher than 700 °C. The first method uses crack width measurements in the thin electrolyte and the second is based on porosity measurements inside the anode support. Anode strain is strongly dependent on:

- the temperature of the RedOx cycle. A "safe" RedOx temperature of 550 °C was calculated and validated. Technologically, it means that below 550 °C no protective gas is needed for such ASE cells.
- the number of RedOx cycles. Successive RedOx cycles show that the process is not reversible but the strain seems to reach a maximum value after ca. 10 cycles.

The difference in the absolute results from both techniques is mainly due to:

- sample preparation: mechanical polishing fills up closed NiO porosity formed at low temperature.
- cell curvature during re-oxidation. This curvature tends to open the electrolyte cracks and is believed to be due to creep of the anode support during re-oxidation.

From porosity measurements, it is possible to estimate the number of RedOx cycles endured by a cell tested in stack conditions, depending on the location inside the cell. This allows a better understanding of the real conditions of cells in a stack test and points to limitations of the stack design.

A re-oxidation strain limit from 0.12 to 0.21% was determined based on finite element modeling and a failure statistics approach. For a constant thickness, this depends on the RedOx temperature and the sample size.

Acknowledgements

Kind acknowledgements are extended to HTceramix® SA (Switzerland) for the materials supply, to the Powder Technology Laboratory in EPFL (Prof. H. Hofmann and C. Morais) for TGA analysis facilities, the Swiss Federal Energy Office and Swisselectric research for financial support (OFEN contract no 152210). The authors are grateful to Dr. H. Lund-Frandsen from Risø (Danish Technological University, DTU) for useful discussions on the creep approach for cell curvature.

References

[1] M. Cassidy, G. Lindsay, K. Kendall, J. Power Sources 61 (1996) 189–192.
[2] R.C. Weast (Ed.), CRC Handbook of Chemistry and Physics, 53rd ed., CRC Press, Cleveland, 1973, B-114 pp.
[3] T. Klemensoe, M. Mogensen, J. Am. Ceram. Soc. 90 (2007) 3582–3588.
[4] D. Sarantaridis, R.J. Chater, A. Atkinson, J. Electrochem. Soc. 155 (2008) B467–B472.
[5] M. Pihlatie, A. Kaiser, P.H. Larsen, M. Mogensen, in: S. Singhal, H. Yokokawa (Eds.), Proceedings of the Solid Oxide Fuel Cells X (SOFC-X), Nara, Japan, ECS Tran., vol. 7(1), 2007, pp. 1501–1510.
[6] D. Sarantaridis, A. Atkinson, in: U. Bossel (Ed.), Proceedings of the 7th European SOFC Forum, Lucerne, Switzerland, 2006, p. P0728.
[7] M. Ettler, G. Blass, N.H. Menzler, Fuel Cells 7 (2007) 349–355.
[8] N.M. Tikekar, T.J. Armstrong, A.V. Virkar, J. Electrochem. Soc. 153 (2006) 654–663.
[9] D. Waldbillig, A. Wood, D.G. Ivey, Solid State Ionics 176 (2005) 847–859.
[10] S. Diethelm, J. Van herle, Z. Wuillemin, A. Nakajo, N. Autissier, M. Molinelli, J. Fuel Cell Sci. Technol. 5 (2008) 031003.
[11] M. Molinelli, D. Larrain, N. Autissier, R. Ihringer, J. Sfeir, N. Badel, O. Bucheli, J. Van herle, J. Power Sources 154 (2006) 394–403.
[12] J. Van herle, D. Larrain, N. Autissier, Z. Wuillemin, M. Molinelli, D. Favrat, J. Eur. Ceram. Soc. 25 (2005) 2627–2632.
[13] D. Larrain, J. Van herle, F. Maréchal, D. Favrat, J. Power Sources 131 (2004) 304–312.
[14] G. Robert, A. Kaiser, E. Batawi, in: M. Mogensen (Ed.), Proceedings of the 6th European SOFC Forum, Lucerne, Switzerland, 2004, p. 193.
[15] A. Faes, A. Hessler-Wyser, D. Presvytes, C.G. Vayenas, J. Van herle, Fuel Cells (2009), accepted for publication.
[16] ABAQUS, Standard User's Manuals, Version 6.7, Hibbitt, Karlsson & Sorensen, Inc., Rhode Island, USA, 2007. www.simulia.com.
[17] A. Atkinson, A. Selçuk, Acta Mater. 47 (1999) 867–874.
[18] A. Atkinson, A. Selcuk, Solid State Ionics 134 (2000) 59–66.
[19] M. Mori, T. Yamamoto, H. Itoh, H. Inaba, H. Tagawa, J. Electrochem. Soc. 145 (1998) 1374–1381.
[20] M. Radovic, E. Lara-Curzio, Acta Mater. 52 (2004) 5747–5756.
[21] W. Weibull, J. Appl. Mech. 18 (1951) 293–297.
[22] ASTM Standard, Standard test method for monotonic equibiaxial flexural strength of advanced ceramics at ambient temperature, Standard ASTM C1499-04, West Conshohocken, 2005.
[23] T. Klemensoe, Relationships between structure and performance of SOFC anodes, Technical University of Danemark, Risoe National Laboratory, Topsoe Fuel Cell, 2005, pp. 103–118.
[24] F.L. Lowrie, R.D. Rawlings, J. Eur. Ceram. Soc. 20 (2000) 751–760.
[25] Z. Wuillemin, N. Autissier, M. Nakajo, M. Luong, J. Van herle, D. Favrat, J. Fuel Cell Sci. Technol. 5 (2008) 0110161–0110169.
[26] L.A. Giannuzzi, F.A. Stevie, Introduction to Focused Ion Beams: Instrumentation, Theory, Techniques And Practice, Springer Science, New York, 2004, pp. 120–124.
[27] J. Malzbender, E. Wessel, R.W. Steinbrech, L. Singheiser, in: E. Lara-Curzio, M.J. Realey (Eds.), Proceedings of the 28th International Conference on Advanced Ceramics and Composites, Cocoa Beach, 2005, p. 378.
[28] F. Gutierrez-Mora, J.M. Ralph, J.L. Routbort, Solid State Ionics 149 (2002) 177–184.
[29] G.M. Kale, D.J. Fray, Metall. Mater. Trans. B 25 (1994) 373–378.
[30] D. Dimos, D.L. Kohlstedt, J. Am. Ceram. Soc. 70 (1987) 531–536.
[31] J. Martinez-Fernandez, M. Jimenez-Melendo, A. Dominguez-Rodriguez, A.H. Heuer, J. Am. Ceram. Soc. 73 (1990) 2452–2456.
[32] D. Gomez-Garcia, J. Martinez-Fernandez, A. Dominguez-Rodriguez, P. Eveno, J. Castaing, Acta Mater. 44 (1996) 991–999.
[33] G.V. Samsonov (Ed.), The Oxide Handbook, 1st ed., IFI/Plenum Corp., New York, 1973, pp. 117–161.
[34] O. Bucheli, M. Molinelli, T. Zahringer, E. Thorn, S. Diethelm, Z. Wuillemin, A. Nakajo, N. Autissier, J. Van herle, in: S. Singhal, H. Yokokawa (Eds.), Proceedings of the Solid Oxide Fuel Cells X (SOFC-X), Nara, Japan, ECS Tran. vol. 7(1), 2007, pp. 123–132.
[35] D. Larrain, J. Van herle, D. Favrat, J. Power Sources 161 (2006) 392–403.